A Comparison of Bone and Bone Surrogate Fragmentation Under Dynamic Compression

Steven J. Pagano[1], **James D. Hogan**[2], **Leslie E. Lamberson**[1*]
[1]Department of Mechanical Engineering and Mechanics, Drexel University, Philadelphia, PA, USA
[2]Department of Mechanical Engineering, The University of Alberta, Edmonton, AB T6G 2R3, Canada

The rate-dependent compressive constitutive response and fragmentation of dry ox cortical bone and cyanoacrylate-based cortical bone surrogate material was investigated for different loading orientations. Uniaxial compressive tests were carried out on both materials for quasi-static loading at 10^{-3} s^{-1} in the logitudinal and transverse directions with respect to the osteon direction or die press, respectively and dynamic loading at 10^{3} s^{-1}. The fragments generated during dynamic loading were analyzed by fitting 2D ellipses of representative distributions using post-mortem optical microscopy. Results show that the bone surrogate material is not as strain-rate sensitive as the ox bone, having an increase in compressive strength of 20-27% with errors of 7% for both from quasi-static to dynamic loading for the transverse and longitudinal directions respectively; while the compressive strength of the ox bone increased 43-66% with errors of 9 and 4% respectively for the same orientations. Resulting bone fragments had a mean size of 266 $\pm$ 28 μm - 410 $\pm$ 19 μm for longitudinal and transverse loading while the bone surrogate produced larger fragments with mean sizes of 431 $\pm$ 14 μm - 694 $\pm$ 25 μm for the same orientations. A power-law relation based on Grady's fragmentation modeling is developed and used to describe the distribution of fragment sizes for both materials. The data fits the power-law relation which implies the relation which implies that the surrogate and dry ox bone behave similar to other brittle materials that the law aims to capture.

1 Introduction

Surrogate bone materials are often used in testing when natural bone is not obtainable, or if more consistent results are required than what would be found in a natural material. One such example is using a surrogate material to evaluate the performance of machine tools used in the medical industry [1], or to obtain diagnostic information such as limb loading or implant behavior [2–4]. One of the primary challenges of developing a surrogate material is the ability to accurately mimic the material properties of natural cortical bone including its rate and orientation response. In addition to having the correct material response, a surrogate material must also be biocompatable in order to not pose a health risk if used as an implant. Examples of this include mechanical fasteners and bone adhesives. Mechanical fasteners are currently used extensively for traumatic injury [5, 6] and adhesives are still actively researched to find the ideal chemical composition [7].

1.1 Material Microstructure

Cortical bone is commonly classified as an organic composite made from three primary components: the osteon, cement lines, and Haversian canals which are interconnected orthogonally by Volkmann canals [8–10]. A schematic of the microstructure is provided in Figure 1. The osteons act as longitudinal support structures within the cortical bone and are bonded together along cement lines, while the Haversian canals are the pathways for interstitial fluid and pass through the center of the osteon [11]. With this configuration, cortical bone can be treated as a transverse isotropic material with a preferential longitudinal direction parallel to the osteon path [12, 13].

The orientation of cortical bone within the human body determines the physiological response during impact events in everyday motion, as well as under extreme loading conditions. It should be noted that while the orientation dependence of the osteon has a large effect on the overall strength of the bone, there are other systems acting in unison that provide support, such as tendons, ligaments, and overall mineral content [14, 15]. For this work, the physiological subcomponents are not considered in the response of the material and the focus is on how the microstructure of cortical bone and a cortical bone surrogate material affects the uniaxial compressive quasi-static and dynamic material response, and resulting fragmentation outcomes.

1.2 Background

Extensive studies on cortical bone have been performed in the past to help characterize the behavior of a natural

*Address all correspondence to this author.

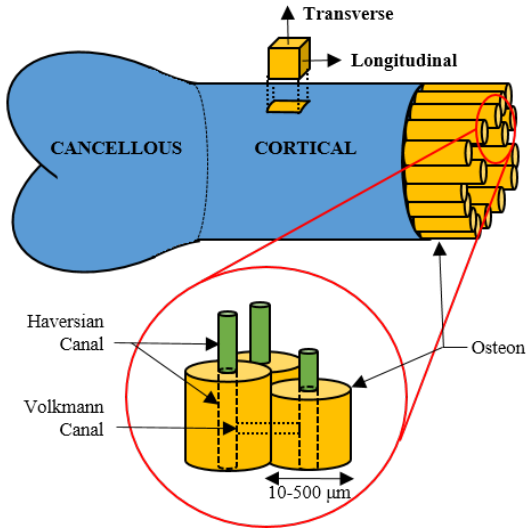

Fig. 1: Schematic of long bone showing cortical region and microstructure. The osteons run parallel to the length of the bone, giving it a preferential direction with Haversian canals in the middle of the osteon.

composite [16–20]. Uniaxial compression testing of cortical bone is typically performed at strain-rates of 10^{-3} s^{-1} to 10^{3} s^{-1} which represents typical physiological loading rates of mammals walking or lightly exercising to high impact events such as falls or automobile accidents. Insight on typical strain-rate behavior of human bone has been gained through in-vivo testing of cortical tibia bone subjected to light and moderate loading activity [16]. Generally speaking, cortical bone is well adapted to the human body by absorbing greater energy during impact loading due to its strain-rate sensitivity. Testing in literature is typically focused on human and bovine cortical bone. These materials are comparable since they have the same microstructure and constitutive relations. Typically bovine bone is used in instances where human bone may be difficult to acquire or poses biological issues such as communicable diseases.

Early fundamental studies on the compressive strength of cortical bone by McElhaney [17] provided insight into its strain-rate behavior. By using a drop-weight compression test on fresh bovine femoral samples at strain-rates of 10^{-3} s^{-1} and 10^{3} s^{-1} he was able to produce compressive strengths of 175 $\pm$ 32 MPa and 365 $\pm$ 38 MPa respectively. Testing on embalmed-dry human femoral bone was 15% weaker at both rates [17]. Conventional uniaxial dynamic compression tests performed with a Kolsky (split-Hopkinson) bar have also been used to characterize cortical bone and to investigate the strain-rate sensitivity behavior [18–20]. A more recent study by Sanborn et al. [18] on human femoral bone yielded similar compressive strengths. Longitudinal strength was measured as 152 $\pm$ 22 MPa at a strain-rate of 10^{-3} s^{-1} which increased to 319 $\pm$ 24 MPa when loaded at a strain-rate of 10^{3} s^{-1}. When loaded in the transverse orientation the strengths decreased to 87 $\pm$ 22 MPa and 179 $\pm$ 26 MPa, respectively [18].

Compression testing at strain-rates of 10^{3} s^{-1} were carried out by Adharapurapu et al. on both fresh and dried bovine femoral cortical bone. They reported average results which show that cortical bone has a longitudinal strength of 459 MPa to 556 MPa for fresh and dried bone, and 296 MPa to 363 MPa for transverse strength in the same conditions [19]. Similar compression testing performed by Ferreira et al. on fresh bovine femoral cortical bone found an ultimate compressive strength of 240 $\pm$ 66.4 MPa to 281 $\pm$ 42.4 MPa for transverse and longitudinal orientations respectively [20].

The spread of results in similar testing highlights the variability in specimens amongst published work for the same mammalian species and bone type (femoral cortical) as well as comparisons to human specimens. The cause for variability can come from physical traits such as specimen age post-mortem [21] or age of the animal prior to harvesting the bone [22]. Variability also can arise from the storage and preservation methods used in other work [23].

The first case of specimen age was investigated by Tennyson et al. for bovine femoral bone in which they found a 33% reduction in stiffness after letting the specimen age in cold water for a span of 14 days [21]. The second case relates to the breakdown of bone that accumulates within the body as it ages. Qualitative studies of the breakdown process were done on human femoral bone by Schaffler et al. by observing the quantity of cracks in specimens with age and noting a large increase in crack density over the age of 40 with a greater density in female specimens [22]. Quantitative data that supports Schaffler's findings was obtained by Zioupos et al. in their research on fracture toughness values, stiffness, and strength of human femoral cortical bone showing a reduction in all three with increase in age [24]. A study of the ideal storage conditions for bone by Stefan et al. shows that if storage is required it is best to freeze fresh bone instead of using a preservation or embalming approach which can chemically alter the bone and either enhance or diminish the mechanical properties [23].

Further research into the fracture properties of both bovine and human cortical bone have been performed to help characterize the behavior with respect to the loading orientation. Notable work in this field came from Bonfield and Behiri who were able to demonstrate the off-axis relation for fracture toughness using fresh-frozen bovine femoral bone that was recovered with Ringer's solution in compact tension tests. Longitudinal loading gave a measured K_c value of 3 MPa$\sqrt{\text{m}}$ which increased to 6.5 MPa$\sqrt{\text{m}}$ in the transverse orientation [25]. The difference in reported K_c values could have implications for resulting fragmentation of bone depending on loading orientation. A thorough review of the fracture behavior of human and bovine specimens has been compiled by Ritchie et al. [12].

1.3 Fragmentation Analysis

A search of existing literature did not find previous studies on the mechanical fragmentation of cortical bone, but rather, was limited to archaeological surveys of mammalian

bone fragments [26, 27].

It has been shown for many brittle materials, including structural ceramics like advanced boron carbide ceramics (B_4C) [28] or aluminum oxynitride (AlON) [29], that fragmentation resulting from dynamic compressive loading produces a range of resulting fragment sizes that can be linked to the failure mechanisms in those materials [30]. The fragmentation of boron carbide ceramics tested dynamically using a Kolsky bar system was investigated by Hogan et al. which found that fragments for hard ceramics can fall into a bimodal distribution. The two modes indicate failure as a structural process (larger fragments) or as a secondary process from Poisson effects that produces smaller fragments [28]. Distributions of fragment sizes will vary depending on the material and applied strain-rate [31]. Ductile materials typically have an exponential distribution while brittle materials can be fit with a power-law distribution [32, 33]. An advantage of using the power-law distribution is that it is not dependent on a characteristic fragment length (typically an average fragment size).

The goal of this work is to characterize and compare a synthetic cortical bone surrogate material to dry ox bone, which has a more realistic material microstructure. This will be done by testing the mechanical response at varying strain-rates and orientations, and analyzing the resulting fragmentation characteristics.

2 Experimental Method

Samples of dry cortical bone from an ox femur and a human cortical bone surrogate made from bovine cortical bone and a resin binder material were tested under quasi-static and dynamic uniaxial compression strain-rates of 10^{-3} and 10^{3} s^{-1}, respectively. The resulting fragmentation characteristics were then analyzed using SEM and optical microscopy with a specially written MATLAB code to measure geometrical features of a representative group of fragments.

2.1 Materials

Dry ox cortical bone was cut from a 20×20×4 mm femoral coupon using a slow-speed diamond wafering blade to 3.5 mm cubic specimens. The surrogate cortical bone material was obtained from BoneSim Laboratories (BoneSim 1800 [1]). The material consists of a proprietary blend of dry bovine cortical bone that has been ground to a particle size of 200 to 750 μm, mixed with a cyanoacrylate based adhesive and allowed to cure while subjected to die pressing to form a transverse isotropic disc. The surrogate material came from the manufacturer as a 50 mm round compressed disc 9.7 mm thick and was similarly cut into 7 mm cubic samples. Orientations were noted during processing with respect to the osteon path and die compaction direction while forming the surrogate. The loading sides of the samples were polished to a high degree of parallelism to ensure uniform loading across the surfaces using a sequence of increasingly finer polishing films, ending with a 3 μm diamond finish.

The loading surface for longitudinal orientation of the bone and surrogate in untested conditions can be seen in Figures 2 and 3. The surrogate has a random dispersion and orientation of bone fragments, with few having the osteon running parallel to the die-press direction as highlighted in Figure 3. There is little similarity in the microstructure of the ox bone and bone surrogate. The bone surrogate lacks the quantity of osteon support structures found in the ox bone and instead has a large quantity of interfacial flaws and pores in the binder material.

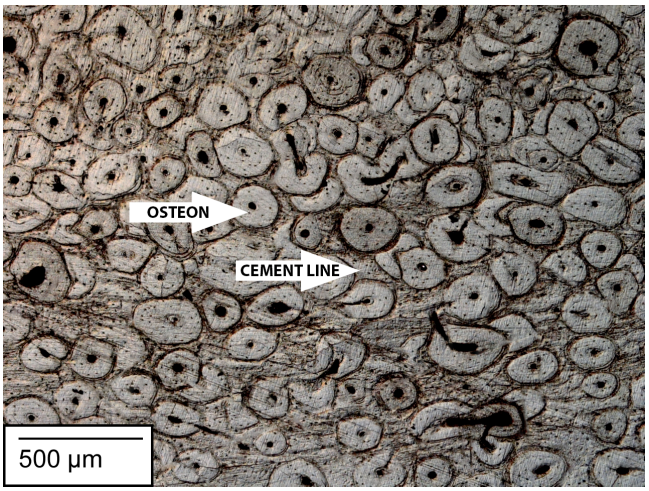

Fig. 2: Microscopy of ox bone in longitudinal orientation showing typical osteon arrangement. Haversian canals are visible as black dots in the center of the osteon.

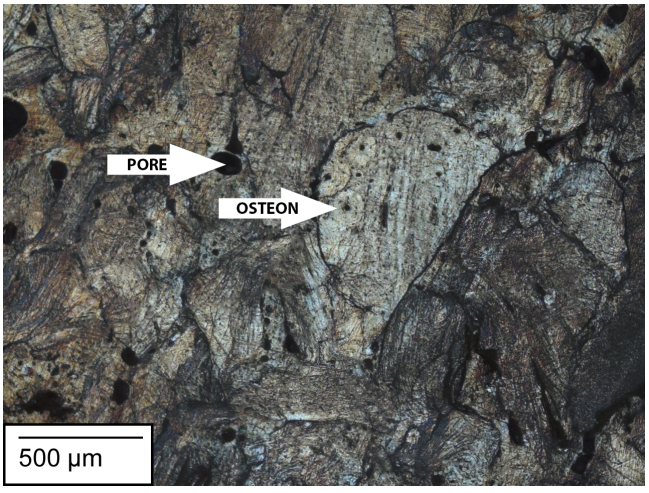

Fig. 3: Microscopy of untested bone surrogate in longitudinal orientation showing random orientation of bone fragments. A collection of osteons and voids in the resin binder is highlighted.

A scanning electron microscope (SEM, FEI XL30) with energy dispersive x-ray spectroscopy (EDX) was used to ex-

amine the surrogate material and identify the elemental composition of regions within the material which are provided in Figure 4 and Table 1.

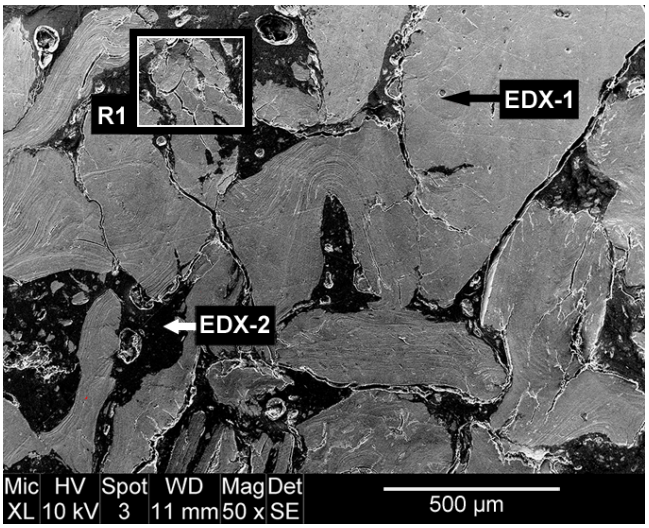

Fig. 4: SEM of typical surface of surrogate material. EDX scans were recorded at the points marked EDX-1 and EDX-2. Region R1 is inspected at higher magnifications in Figure 5.

EDX measurements were recorded for a period of 100 s at the locations marked 'EDX-1' and 'EDX-2' in Figure 4. The location 'EDX-1' was identified as an osteon in Figure 3 and 'EDX-2' appeared as a distinct region separate from the previous measurement and is believed to be the resin binder. The osteon identified in Figure 4 was found to have the majority of its weight percentage (Wt. %) as calcium and phosphorus, which is typical of bone. The darker regions in Figure 4 had a significantly smaller weight percent of calcium and phosphorus with the majority of its composition coming from carbon. The contrast provided by the SEM allowed for an identification of 78% cortical bone content with the remainder being the cyanoacrylate based adhesive acting as a binder. The granular bone particles were found to have a random orientation within the binder with respect to the osteon path and surrogate press direction.

Table 1: EDX weight percentage measurements for two distinct regions in surrogate material for 100 s (refer to Figure 4).

Location	Element [Wt. %]				
	C	O	P	Ca	Other*
EDX-1	11.19	11.05	23.95	50.28	3.53
EDX-2	84.86	1.61	5.62	4.86	3.05

*Other includes $<$1.25% of Mg, Mn, and Na

Extensive pre-existing damage in the form of cracks was found on the ground bone fragments in the surrogate material while the binder showed numerous voids. A region designated 'R1' in Figure 4 was identified as having damage and is shown in more detail in Figure 5. The inset shows that at higher magnifications there is evidence of crack bridging which is explained in greater detail by Ritchie for metals, ceramics, and composites [34] and again in his more recent review of cortical bone [12] where the later is bridged by collagen fibers within the tissue. Damage of this nature was typical throughout the surrogate.

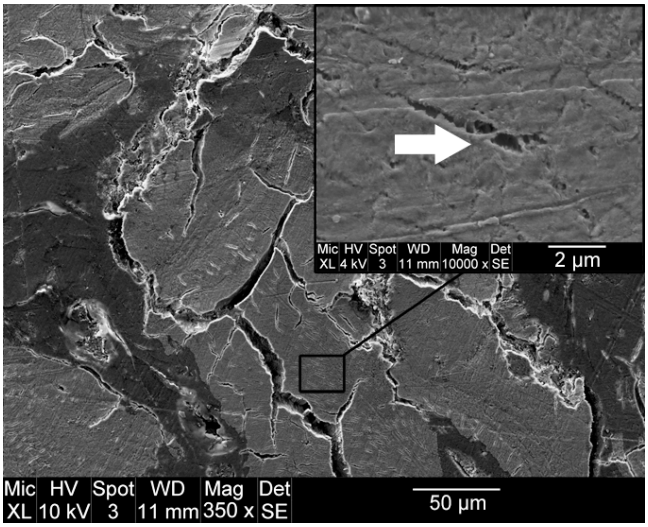

Fig. 5: SEM of bone surrogate region 'R1' (Figure 4) illustrating pre-existing damage. *Inset* shows evidence of crack bridging.

2.2 Mechanical Testing

Both materials were subjected to uniaxial compression using a Shimadzu AG-IS 50 kN loading frame at a loading rate of 0.15 mm s^{-1} (strain-rate or $\dot{\varepsilon}$ of 10^{-3} s^{-1}) in longitudinal and transverse orientations. Dynamic uniaxial compression was performed for both materials and orientations with a Kolsky bar at a strain-rate of 10^{3} s^{-1}. A schematic of the bar arrangement is shown in Figure 6. Its principle of operation is through the propagation of a stress pulse. Two round hardened steel bars known as the incident and transmitted bar are supported by linear bearings. A sample is placed between the two bars and a stress pulse is generated in the incident bar by impacting it with a striker, typically from a gas gun. The governing equations for a Kolsky bar are provided in Equations 1-3. Strain-rate is determined through the reflected strain in the incident bar ε_R with the time component coming from the longitudinal wave speed of the bar, denoted c_b. The length is normalized by the sample length in the loading direction, L_0. By integrating the strain-rate over the loading time of the test the strain for the sample, $\varepsilon(t)$ can be calculated. Finally, the strain recorded in the transmitted

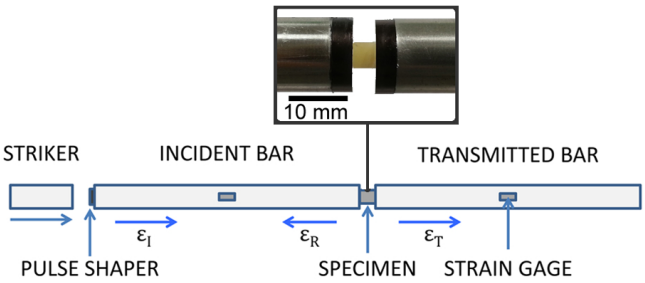

Fig. 6: Kolsky bar arrangement for dynamic uniaxial compression. Inset: Ox bone sample between incident and transmitted bar.

bar can be used with the Young's modulus of the bar, E_b and ratio of bar area to sample area, A_b/A_0 to calculate the stress, $\sigma(t)$. In order to reach a state of uniform loading the stress pulse needs to traverse the length of the sample at least three times (incident pulse with first and second reflections within the sample). For the size of the samples used in this experiment and estimating the material wave speed at 2990 m/s for bone would give a typical delay of 3.5 to 7 µs for the ox bone and bone surrogate respectively before reaching the uniform loading state. More details on this type of testing can be found in [35, 36].

$$\dot{\varepsilon}(t) = -\frac{2c_b}{L_0}\varepsilon_R(t) \tag{1}$$

$$\varepsilon(t) = \int_0^t \dot{\varepsilon}(t)dt \tag{2}$$

$$\sigma(t) = \frac{E_b A_b}{A_0}\varepsilon_T(t) \tag{3}$$

A 150 mm long 12.7 mm diameter striker was loaded into a light-gas gun to provide the input pulse when incident upon the Kolsky bar. The sample was placed between a pair of aluminum oxide (Al_2O_3) platens located between the incident and transmission bars. A small amount of silicone grease was used between the bars, platens, and sample to reduce interface friction between the sample and platens. A small piece of copper, 4.2 mm round by 0.5 mm thick was placed in front of the incident bar as a pulse shaper to extend the loading time to reach a uniform stress state [35].

Data collection was performed with a 200 MHz LeCroy HDO 4024 oscilloscope in conjunction with a pair of half-bridge circuits instrumented on each bar. The strain gages are bonded to each bar 180° apart to allow cancellation of bending within the bar and provide pulse characterization as the stress wave propagates along the bar. The half-bridge was made up of a pair of Vishay Micro-Measurement EK-06-250BF-10C/W 1000 Ω strain gages, matching resistors, and a potentiometer to balance the bridge. When excited with a 30 V source the half bridge circuits had a combined load of 60 mA.

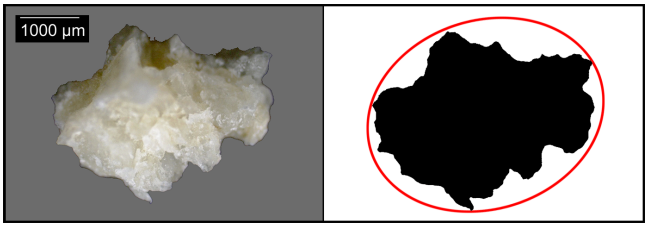

Fig. 7: (L) Optical microscopy of typical surrogate fragment. (R) Processed and fit with idealized ellipse: 3.9 mm, 3.2 mm, 1.25 (Major Axis, Minor Axis, $\mathcal{AR}$).

2.3 Fragmentation Analysis

A containment box made from 2 mm thick polycarbonate was placed around the sample section of the Kolsky bar and used to contain the fragments generated during dynamic loading. Care was taken to collect the majority of fragments and it is recognized that not all fragments may have been recovered due to small openings in the containment box for the bars to pass through. Results of this collection are provided in Table 3. It should be noted that the aluminum oxide platens were recovered completely intact with no signs of damage and all fragments are believed to be from the tested specimen. The fragments were then imaged using a Zeiss Axiocam MRc with a low-power objective lens and analyzed using MATLAB's Image Processing Toolbox to determine geometric parameters [37].

The analysis process consists of first converting the images to grayscale in order to adjust contrast and sharpness of the fragment outline then further converted to a binary image. An idealized ellipse is fit to each fragment, which is then used to determine parameters such as major and minor axis length. The major axis length is used for the characteristic size L of a fragment and the ratio of the two axis defines the shape or aspect ratio ($\mathcal{AR}$). The area of each fragment was also measured using contiguous pixel mapping. An example of a surrogate fragment is shown in Figure 7 along with a typical analysis of the surface. Details for this technique can be found in [38].

3 Results

The following section outlines the results of mechanical testing and fragmentation analysis. Samples of each material were tested in the longitudinal and transverse orientation for both uniaxial quasi-static and dynamic loading. The resulting fragments were then analyzed for geometric parameters to better understand the nature of the failure and fragmentation process.

3.1 Uniaxial Compressive Response

A summary of the mechanical testing results are provided in Table 2. The mechanical response for both materials and orientations under quasi-static loading is provided in Figure 8. The dry ox bone was found to have a quasi-static compressive strength 3 to 4 times greater than the surrogate material. A reason for this dramatic difference may be due to

Table 2: Summary of results from quasi-static and dynamic uniaxial compression testing, reported values are averaged from two similar tests with standard deviation (± SD).

Material	Orientation	Strain Rate $\dot{\varepsilon}$, [s^{-1}]	Compressive Max Stress σ_c, [MPa]
Ox Bone	Longitudinal	10^{-3}	336 ± 6
		2700 ± 150	559 ± 23
	Transverse	10^{-3}	244 ± 22
		2400 ± 150	350 ± 34
Surrogate	Longitudinal	10^{-3}	84 ± 5
		2000 ± 90	101 ± 7
	Transverse	10^{-3}	82 ± 9
		1700 ± 20	104 ± 7

the fact that the surrogate bone aims to match fresh cortical bone, and not the dry cortical bone tested in this work which is more brittle than a fresh specimen. The dry ox bone also had a microstructure that favors the longitudinal direction, whereas the surrogate did not have this orientational dependency. The bone was found to have a different mechanical response between the longitudinal and transverse orientation, which is attributed to the inherent anisotropy. Longitudinal strength of the dry cortical bone was 38% higher than transverse strength at quasi-static loading rates and 60% higher at strain-rates of 10^3 s^{-1}. The surrogate does not appear to show a significant difference between loading orientations despite the die-pressing, perhaps due to its random bone fragment orientations and relatively uniform distribution, and hence nearly isotropic microstructure.

Stress history or $\sigma_c(t)$ is provided for the dynamic tests in Figure 9. The ox bone had a peak compressive strength 66% greater in the longitudinal orientation and 43% greater in the transverse orientation for $\dot{\varepsilon} = 10^3$ s^{-1} compared to the quasi-static loading. The surrogate had similar compressive strengths when loaded longitudinally in dynamic testing as compared to the transverse orientation with overlapping error between the two results. The strain-rate sensitivity was also less than what was found with the ox bone, having a peak compressive strength increase of 20 to 27% over the quasi-static values when tested at $\dot{\varepsilon} = 10^3$ s^{-1}. Stress history of dynamic testing normalized by dynamic longitudinal ox bone is provided in Figure 10.

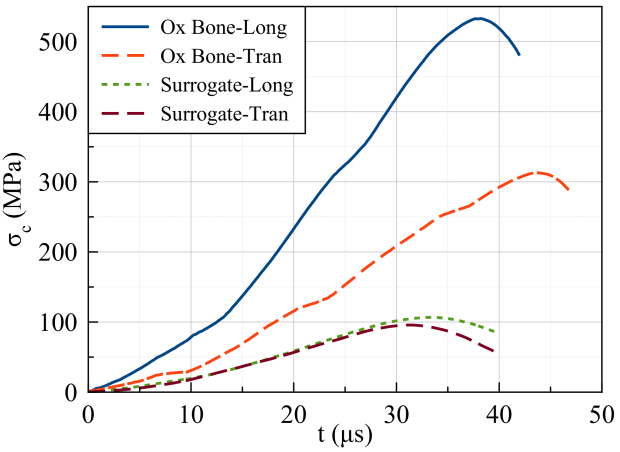

Fig. 9: Stress history of single representative test during dynamic loading ($\dot{\varepsilon} = 10^3$ s^{-1}) for ox bone and surrogate in longitudinal and transverse loading, portion of unloading is shown to illustrate peak compressive stress.

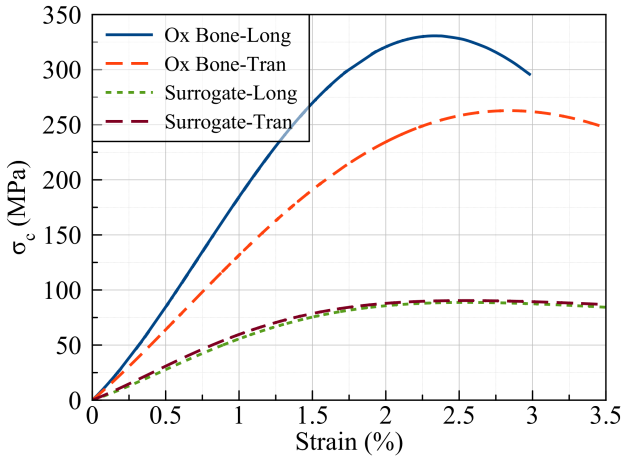

Fig. 8: Characteristic results for quasi-static ($\dot{\varepsilon} = 10^{-3}$ s^{-1}) uniaxial compressive response of ox bone and bone surrogate in both the longitudinal and transverse orientation.

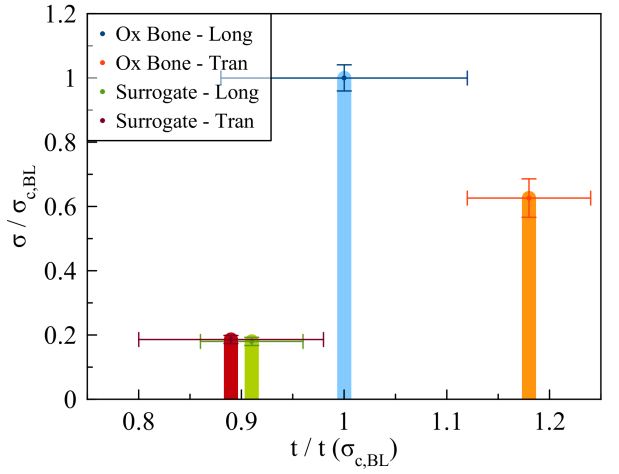

Fig. 10: Dynamic maximum strength and loading time normalized by dynamically loaded ($\dot{\varepsilon} = 10^3$ s^{-1}) longitudinal ox bone data.

3.2 Fragmentation Analysis

The fragments generated during dynamic loading were collected and weighed to get a sense of how much material was recovered from the original sample. The surrogate material had a recovered mass of 43-49% for longitudinal and transverse loading and 45-81% of the bone was recovered for the same orientations Fragments were then imaged and processed using the method described in the experimental procedure. Results of the processed data were compared between individual tests as well as combining the fragments from similar tests. Scatter plots of the distribution were used to compare the individual tests to the combined data and it was found that both data sets produced similar distributions. For this reason it is believed that less than 50% of the recovered material still constitutes a representative population. In order to increase the fidelity of our data, the combined data sets are used for the rest of the analysis which results in an increase of representative population for each material and orientation with respect to loading while not effecting the overall distributions. Fragment characteristics for each material set are provided in Table 3. It should be noted that the ox bone had a smaller data set which is related to the smaller size of the original sample as compared to the bone surrogate (see Section 2.1).

Scatter plots for the distribution of fragment shape and size are provided in Figures 11 and 12. The distribution of

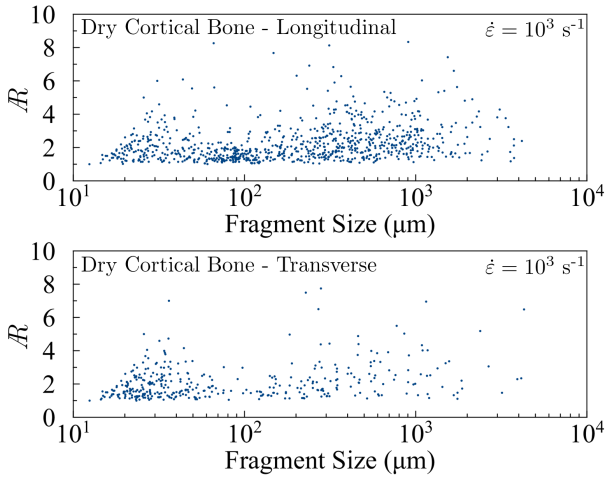

Fig. 11: Ox bone fragment size characteristics from dynamic loading ($\dot{\varepsilon} = 10^3$ s^{-1}).

fragments for the ox bone was found to contain both a similar amount of small (sub-100 μm) and large fragments for both the longitudinal and transverse orientation as evidenced by the fragment size characteristics. Fragments generated during the dynamic loading of the surrogate fell into two primary size regimes for both longitudinal and transverse orientations. Smaller fragments were generated with a typical size of 50 to 100 μm, and larger fragments on the order of 1 mm which represent the family size for structurally dependent failure and is the focus of this work.

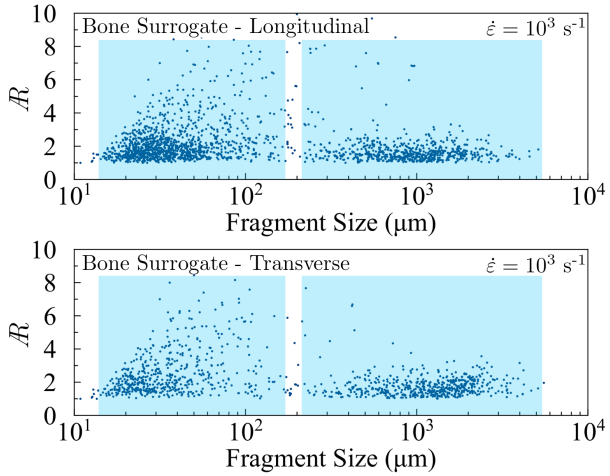

Fig. 12: Bone surrogate fragment size characteristics from dynamic loading ($\dot{\varepsilon} = 10^3$ s^{-1}). Shaded regions highlight the two fragment size regimes.

To gain more insight on the fragmentation, the size of the fragments was plotted against different distributions including exponential, log-normal, Weibull, Rayleigh and a power-law. It was found that the data best fit a power-law distribution as these are more suitable for brittle materials that fragment into a range of sizes. Previous work by Bergstrom on static testing of glass spheres [39] and torsional Hopkinson bar testing of ferroelectric ceramics by Costin [40] was used by Grady to formulate a power-law fit specifically for brittle materials [41] which has the form,

$$G(L) = \frac{1}{1 + \left(\frac{L_i - L_{min}}{a}\right)^b}, \tag{4}$$

where a is a scaling parameter to normalize the fragment length and is related to the applied strain-rate where higher strain-rates have a smaller value. The parameter b is for shape fitting and has a reducing absolute value for higher strain-rates. The distributions for each dynamic test are provided in Figure 13.

4 Discussion

4.1 Uniaxial Compressive Response

The uniaxial compression strength testing of the cortical bone was found to be similar to other published data for both quasi-static and dynamic loading when taking into account the variability (species [17], age [21], storage conditions [23]) of specimens among published work. A comparison of the longitudinal compressive strength and strain-rate from present work and published data is provided in Figure 14. Early studies from McElhaney on embalmed human femoral bones show a relatively low strength [17], owed likely to the embalming process and chemicals used, as demonstrated by Stefan et al. [23]. Testing of fresh bovine

Table 3: Characteristics of fragments larger than 100!µm generated during dynamic uniaxial compressive loading. Standard error of the mean (± SEM) is provided for the fragment size, $\mathcal{R}$, and area.

Material	Orientation	Fragment Quantity	Mean Size [µm]	Mean $\mathcal{R}$	Mean Area [mm^2]	Mass Recovered [%]
Ox Bone	Longitudinal	865	410 ± 19	2.29 ± 0.04	0.16 ± 0.02	45
	Transverse	370	266 ± 28	2.15 ± 0.06	0.11 ± 0.03	81
Surrogate	Longitudinal	2001	431 ± 14	2.22 ± 0.04	0.29 ± 0.02	43
	Transverse	1152	694 ± 25	2.31 ± 0.05	0.53 ± 0.03	49

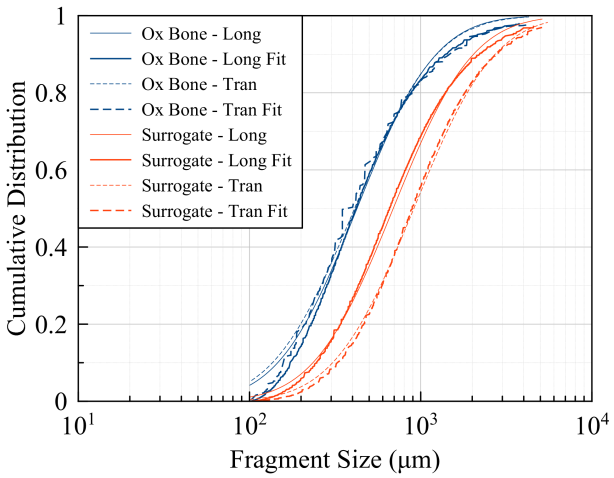

Fig. 13: Cumulative distributions of fragment size for $L \geq 100$ µm of surrogate material from dynamic loading ($\dot{\varepsilon} = 10^3$ s^{-1}). Experimental data is fit with power-law distributions from Equation 4. For scaling parameters see Table 4.

Table 4: Scaling parameters used in Equation 4. Parameter a normalizes the fragment length and b shapes the profile. The absolute value of each parameter decreases with increasing strain-rate.

Material	Orientation	Parameters	
		a (µm)	b
Ox Bone	Longitudinal	320	-1.55
	Transverse	300	-1.40
Surrogate	Longitudinal	560	-1.65
	Transverse	795	-1.80

femoral bone by Ferreria et al. achieved a lower strength than that of Adharapurapu [19, 20] which is expected for a wet or fresh specimen that isn't as stiff as a dry bone sample. The dry bovine femoral bone that Adharapurapu investigated had a compressive strength that matched our ox bone at strain-rates of 10^3 s^{-1} and was 44% weaker than the ox bone at quasi-static rates of 10^{-3} s^{-1}. The difference between strength at lower loading rates is not of major concern as there is a difference in species and likely age of specimen both pre- and post-moretem.

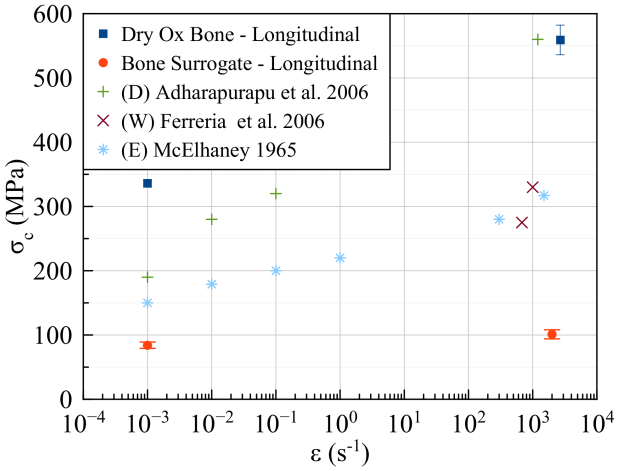

Fig. 14: A comparison of longitudinal compressive strength and applied strain-rate from present work and published data. (D) dry bovine femur, (W) wet (fresh) bovine femur, (E) embalmed-dry human femoral [17, 19, 20].

The testing of cortical bone provided a baseline to compare the behavior of the surrogate material, where the bone exhibits anisotropic behavior due to the microstructure highlighted in Figure 1. The surrogate bone however was found to be more homogeneous isotropic as evidenced in Figure 3 and 4. Cortical bone was shown to have an orientation dependency when tested both quasi-statically and dynamically with the longitudinal direction having a higher load bearing capacity owed to the preferential osteon direction. A strain-rate dependency was found in dynamic testing as well with significant compressive stress increases over the quasi-static values of 67% seen for longitudinal orientation and 43% in transverse with an error of 4 and 9% respectively.

The quasi-static compressive strength for the surrogate were shown to be weaker than the ox femur. However, this

is expected as the bone was in a dry form and more brittle than freshly procured bone samples that the surrogate aims to simulate. Similar work by Adharapurapu et al. [19] also shows that dry bone is capable of supporting more load than fresh (or wet) bone due to the increase in stiffness as moisture is removed leading to a more brittle material. A rate dependency was found for the surrogate material with respect to the peak stress. When loaded dynamically an overall increase in compressive strength of 27% was found for the surrogate in the longitudinal orientation with transverse being slightly and not statistically significant enough to claim a real difference exists. The bone surrogate aims to be a consistent homogenized material with low variability between testing. While the surrogate had less deviation from the mean values, the overall strength was weaker and thus the coefficient of variation is used as a means of measuring the consistency of testing results. The quasi-static testing of ox bone had a coefficient of variation for longitudinal and transverse loading of 0.02 and 0.09 compared to the bone surrogate of 0.06 and 0.11. The dynamic testing was marginally better for the surrogate material having a value of 0.07 for both longitudinal and transverse orientations. This metric was similar for ox bone under dynamic compression at 0.04 for longitudinal and 0.09 for transverse. It was expected that the coefficient of variation should be lower for the bone surrogate which was not the case even though standard deviations of strength were smaller than the ox bone.

Pre-existing damage within the untested surrogate material can be observed in region R1 as shown in Figure 5. A large quantity of flaws with a length of 2-4 μm are visible. At higher magnification there is evidence of crack bridging at the flaw which is typical of cortical bone [12]. Damage of this magnitude is common throughout the bone regions in the material and is attributed to mechanical processing of the bone (grinding and die pressing) during the manufacturing of the material. A possible reason for the smaller rate dependency of the surrogate is due to the activation of numerous flaws in the surrogate that do not exist in the natural bone. Flaws exist along the interfaces between the resin binder and the bone due to poor adhesion or as defects such as pores in the bulk of the resin binder which will be investigated further in the next section.

4.2 Fragmentation Analysis

An analysis of the bone fragments shows that the distribution of size is fairly even between small and large fragments (Figure 11). One possibility for the spread of fragment sizes is that the failure mechanism lies along the cement lines of the osteon where fracture occurs due to localized plasticity and pore collapse. Fragmentation generates longer fragments during loading on the order of 500-1000 μm with smaller fragments being generated from the typical spacing of Volkmann canals that connect adjacent Haversian canals perpendicular to the osteon [10]. We hypothesize that the canal systems act as points for the crack to change direction and break off a larger osteon structure. Evidence of this behavior is provided in Figure 15 and Figure 16. Interestingly, the fragments analyzed in Figure 15 show the different canal paths exposed. Previous work on the fracture mechanics of cortical bone [12, 25] suggested that the cement lines between osteons provides the weak path that the crack would follow. Since the canal systems are exposed, this would suggest that the osteon split during the fracture process to expose the inner surfaces of the osteon canal system.

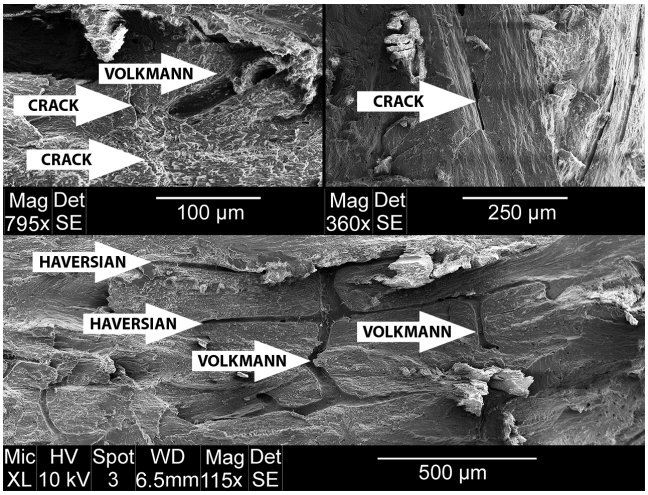

Fig. 15: SEM image of fragments generated from dynamic loading of dry ox bone in the longitudinal orientation. Splitting of the osteon revealed the internal canal system.

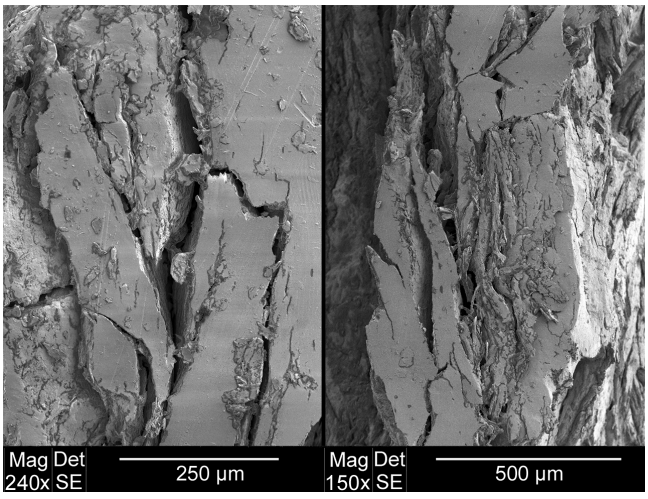

Fig. 16: SEM image of fragments generated from dynamic loading of dry ox bone in the transverse orientation. The extensive crushing shown is from the surface of a single fragment. The broken texture was present on all fragments with no visible indication of a canal system.

The transverse loading of dry ox bone produced an even distribution of fragments that suggests failure of the osteon

through a comminution behavior before reaching a weak cement line that deflects the crack from perpendicular to parallel to the osteon, consequently producing a more uniform distribution of fragment sizes [42]. Figure 16 shows evidence of the comminution behavior. After studying multiple transverse fragments there was no definitive evidence of osteon splitting like what was seen in the longitudinal fragments.

The characteristic length of a typical surrogate fragment was found to fall within two regimes as shown in Figure 12. Larger fragments, on the order of 1000 μm are believed to be generated through structural failure while smaller fragments with a typical length of 50 μm are formed from secondary processes. It is likely that smaller fragments resulted from the crushing of osteons as few instances of preferential directions could be found in microscopy (such as the longitudinal bone section shown in Figure 3). An analog to this behavior is typically seen in brittle materials such as ceramics or rocks as transgranular fractures [30, 38]. SEM images of the surrogate could not discern a difference between longitudinal and transverse loading. A common finding was a large number of pores existing along the interface of the ground bone and binder as shown in Figure 17. The presence of the pores suggests that there was a lack of proper wetting of the ground bone by the binder phase leading to a weak interaction of the adhesive and bone. The quantity and size of pores was not consistent, with sizes ranging from a few microns to over 100 μm.

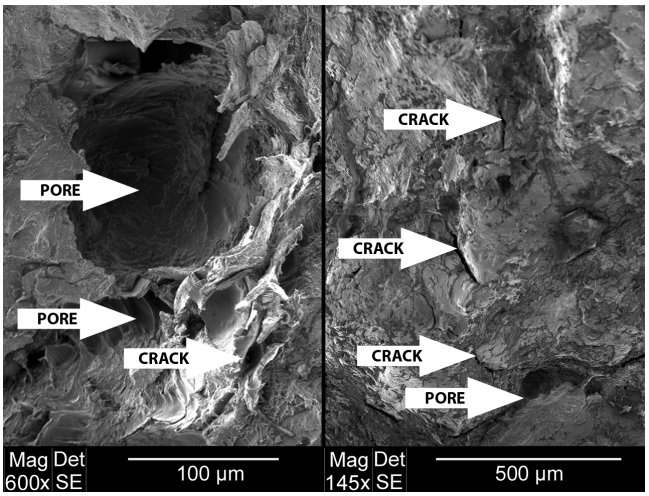

Fig. 17: SEM image of fragments generated from dynamic loading of bone surrogate in longitudinal orientation (transverse is similar). A large number of pores exist along the interface of the bone and adhesive, leading to failure from crack growth.

The two-parameter power-law fit of the distribution shows that at higher applied strain-rates there is a decrease in the size parameter a. The decrease is due to the resulting fragments being smaller at higher compressive loads. The absolute value of the parameter b also decreased at higher strain-rates for similar reasons, providing a better shape-fit of the distribution. These parameters are expected to be refined and updated as more experimental data is made available for varying strain-rates and materials such as other bone surrogates or natural bone under different conditioning (specimen age for instance). This work shows that applicability of Grady's power-law is not limited to brittle materials like structural ceramics and glass, but can in fact be use for natural materials like cortical bone.

5 Conclusion

Our work examined the uniaxial compressive response and dynamic fragmentation of a cortical bone surrogate material and dry ox bone. Maximum compressive strength values for quasi-static loading of ox bone were 336 MPa and 244 MPa for longitudinal and transverse orientations while dynamic loading saw an increase to 559 MPa and 350 MPa. These results show that there is a strain-rate sensitivity to the cortical bone with strength increases of 43% to 66% when tested dynamically for the two loading directions. The bone surrogate did not show the same degree of strain-rate sensitivity as the dry bone due to the lack of structure exhibited by the ox bone. Quasi-static maximum stress values for the bone surrogate in longitudinal and transverse orientations were 84 MPa and 82 MPa respectively. The maximum compressive strength increased slightly when tested dynamically to 101 MPa and 104 MPa for longitudinal and transverse, an increase of 20% to 27% over quasi-static values. Interestingly, there is only a 2% to 6% difference between longitudinal and transverse orientations for both loading rates. The ox bone had an increase in maximum stress when loaded longitudinally for both quasi-static and dynamic of 49% and 60% as compared to the transverse orientation. The similar response between loading orientations highlights the homogeneous material structure as compared to ox bone which has a structure defined by the osteon growth direction.

The analysis of the fragments produced during dynamic loading show a difference between the two materials. Dynamic uniaxial loading of the dry ox bone produced fragments through splitting of the osteon. When loaded transversely the resulting fragments came from crushing of the osteon structure. The surrogate material produced larger fragments than the ox bone in terms of a major axis length and projected surface area. It is somewhat intuitive to expect this knowing that the surrogate is formed from ground bone glued together and failure along the glue joint is more likely than further comminution of the bone. Fragmentation was exacerbated by the presence of pores and lack of interaction between the adhesive and bone. This work provided insight into the fragmentation of cortical bone. Further research of bone and bone surrogate materials can assist with the medical diagnosis of bone fractures by understanding the size of expected bone fragments from the applied loading.

References

[1] Blakemore, D., 2013. *BoneSim 1800 Cortical Bone Analog*. BoneSim Laboratories, Cassopolis, Michigan.

[2] Agneskirchner, J., Freiling, D., Hurschler, C., and Lobenhoffer, P., 2006. "Primary stability of four different implants for opening wedge high tibial osteotomy". *Knee Surgery, Sports Traumatology, Arthroscopy,* **14**(3), pp. 291–300.

[3] Cristofolini, L., Viceconti, M., Cappello, A., and Toni, A., 1996. "Mechanical validation of whole bone composite femur models". *Journal of Biomechanics,* **29**(4), pp. 525–535.

[4] Heiner, A., and Brown, T. D., 2001. "Structural properties of a new design of composite replicate femurs and tibias". *Journal of Biomechanics,* **34**(6), pp. 773–781.

[5] Peindl, R., Zura, R., Vincent, A., Coley, E., Bosse, M., and Sims, S., 2004. "Unstable proximal extraarticular tibia fractures: a biomechanical evaluation of four methods of fixation". *Journal of Orthopaedic Trauma,* **18**(8), pp. 540–545.

[6] Siffri, P., Peindl, R., Coley, E., Norton, J., Connor, P., and Kellam, J., 2006. "Biomechanical analysis of blade plate versus locking plate fixation for a proximal humerus fracture: comparison using cadaveric and synthetic humeri". *Journal of Orthopaedic Trauma,* **20**(8), pp. 547–554.

[7] Farrar, D., 2012. "Bone adhesives for trauma surgery: A review of challenges and developments". *International Journal of Adhesion and Adhesives,* **33**, pp. 89–97.

[8] Rho, J., Kuhn-Spearing, L., and Zioupos, P., 1998. "Mechanical properties and the hierarchical structure of bone". *Medical Engineering & Physics,* **20**(2), pp. 92–102.

[9] Katz, J., 1981. "Composite material models for cortical bone". *Mechanical Properties of Bone,* **45**, pp. 171–184.

[10] Cooper, D., Turinsky, A., Sensen, C., and Hallgrimsson, B., 2003. "Quantitative 3d analysis of the canal network in cortical bone by micro-computed tomography". *The Anatomical Record Part B: The New Anatomist,* **274**(1), pp. 169–179.

[11] Currey, J., 1982. "Osteons in biomechanical literature". *Journal of Biomechanics,* **15**(9), p. 717.

[12] Ritchie, R., Kinney, J., Kruzic, J., and Nalla, R., 2005. "A fracture mechanics and mechanistic approach to the failure of cortical bone". *Fatigue & Fracture of Engineering Materials & Structures,* **28**(4), pp. 345–371.

[13] Burr, D., 2010. "Cortical bone: a target for fracture prevention?". *The Lancet,* **375**(9727), pp. 1672–1673.

[14] Carter, D., and Spengler, D., 1978. "Mechanical properties and composition of cortical bone". *Clinical Orthopaedics and Related Research,* **135**, pp. 192–217.

[15] Wang, T., and Feng, Z., 2005. "Dynamic mechanical properties of cortical bone: The effect of mineral content". *Materials Letters,* **59**(18), pp. 2277–2280.

[16] Milgrom, C., Finestone, A., Levi, Y., Simkin, A., Ekenman, I., Mendelson, S., Millgram, M., Nyska, M., Benjuya, N., and Burr, D., 2000. "Do high impact exercises produce higher tibial strains than running?". *British Journal of Sports Medicine,* **34**(3), pp. 195–199.

[17] McElhaney, J., 1966. "Dynamic response of bone and muscle tissue.". *Journal of applied physiology,* **21**(4), pp. 1231–1236.

[18] Sanborn, B., Gunnarsson, C., Foster, M., Moy, P., and Weerasooriya, T., 2014. Effect of loading rate and orientation on the compressive response of human cortical bone. Tech. rep., DTIC Document.

[19] Adharapurapu, R., Jiang, F., and Vecchio, K., 2006. "Dynamic fracture of bovine bone". *Materials Science and Engineering: C,* **26**(8), pp. 1325–1332.

[20] Ferreira, F., Vaz, M., and Simoes, J., 2006. "Mechanical properties of bovine cortical bone at high strain rate". *Materials Characterization,* **57**(2), pp. 71–79.

[21] Tennyson, R., Ewert, R., and Niranjan, V., 1972. "Dynamic viscoelastic response of bone". *Experimental Mechanics,* **12**(11), pp. 502–507.

[22] Schaffler, M., Choi, K., and Milgrom, C., 1995. "Aging and matrix microdamage accumulation in human compact bone". *Bone,* **17**(6), pp. 521–525.

[23] Unger, S., Blauth, M., and Schmoelz, W., 2010. "Effects of three different preservation methods on the mechanical properties of human and bovine cortical bone". *Bone,* **47**(6), pp. 1048–1053.

[24] Zioupos, P., and Currey, J., 1998. "Changes in the stiffness, strength, and toughness of human cortical bone with age". *Bone,* **22**(1), pp. 57–66.

[25] Behiri, J., and Bonfield, W., 1989. "Orientation dependence of the fracture mechanics of cortical bone". *Journal of Biomechanics,* **22**(8), pp. 863–872.

[26] Todd, L., and Rapson, D., 1988. "Long bone fragmentation and interpretation of faunal assemblages: approaches to comparative analysis". *Journal of Archaeological Science,* **15**(3), pp. 307–325.

[27] Morlan, R., 1994. "Bison bone fragmentation and survivorship: a comparative method". *Journal of Archaeological Science,* **21**(6), pp. 797–807.

[28] Hogan, J., Farbaniec, L., Shaeffer, M., and Ramesh, K., 2015. "The effects of microstructure and confinement on the compressive fragmentation of an advanced ceramic". *Journal of the American Ceramic Society,* **98**(3), pp. 902–912.

[29] Paliwal, B., Ramesh, K., and McCauley, J., 2006. "Direct observation of the dynamic compressive failure of a transparent polycrystalline ceramic (alon)". *Journal of the American Ceramic Society,* **89**(7), pp. 2128–2133.

[30] Ramesh, K., Hogan, J., Kimberley, J., and Stickle, A., 2014. "A review of mechanisms and models for dynamic failure, strength, and fragmentation". *Planetary and Space Science*.

[31] Grady, D., 2009. "Dynamic fragmentation of solids". *Shock Waves Science and Technology Reference Library,* **3**.

[32] Åström, J., 2006. "Statistical models of brittle fragmentation". *Advances in Physics,* **55**(3-4), pp. 247–278.

[33] Grady, D., 2010. "Length scales and size distributions in dynamic fragmentation". *International Journal of Fracture,* **163**(1-2), pp. 85–99.

[34] Ritchie, R., 1988. "Mechanisms of fatigue crack propagation in metals, ceramics and composites: role of crack tip shielding". *Materials Science and Engineering: A,* **103**(1), pp. 15–28.
[35] Chen, W., and Song, B., 2010. *Split Hopkinson (Kolsky) bar: design, testing and applications*. Springer.
[36] Ramesh, K., 2008. "High rates and impact experiments". In *Springer Handbook of Experimental Solid Mechanics*. Springer, pp. 929–960.
[37] MATLAB, 2015. *version 8.5.0 (R2015a)*. The MathWorks Inc., Natick, Massachusetts.
[38] Hogan, J., Rogers, R., Spray, J., and Boonsue, S., 2012. "Dynamic fragmentation of granite for impact energies of 6–28J". *Engineering Fracture Mechanics,* **79**, pp. 103–125.
[39] Bergstrom, B., Sollenberger, C., and Mitchell Jr, W., 1961. "Energy aspects of single particle crushing". *Trans. AIME,* **220**, pp. 367–372.
[40] Costin, L., and Grady, D., 1984. Dynamic fragmentation of brittle materials using the torsional kolsky bar. Tech. rep., Sandia National Labs., Albuquerque, NM (USA).
[41] Grady, D., 2008. "Fragment size distributions from the dynamic fragmentation of brittle solids". *International Journal of Impact Engineering,* **35**(12), pp. 1557–1562.
[42] Nalla, R., Stölken, J., Kinney, J., and Ritchie, R., 2005. "Fracture in human cortical bone: local fracture criteria and toughening mechanisms". *Journal of Biomechanics,* **38**(7), pp. 1517–1525.